Emission Source Microscopy Technique for EMI Source Localization

Pratik Maheshwari, and Hamed Kajbaf, *Member, IEEE*, Victor V. Khilkevich, *Senior Member, IEEE*, and David Pommerenke, *Fellow, IEEE*

***Abstract*—For large, complex systems with multiple sources at the same frequency, localizing the sources of radiation often proves difficult. This paper presents an emission source microscopy (ESM) technique derived from synthetic aperture radar (SAR) to localize radiating sources on a PCB. Near-field scanning provides limited information about the components contributing to far-field radiation. This paper presents the source localization methodology, supported by simulation and measurement results. After localizing the sources, the far-field contribution and the total radiated power from each individual source can be estimated. The results show that the proposed method can distinguish between multiple radiating sources on a complex PCB.**

***Index Terms*—source localization, EMI, radiation sources, near-field scanning, emission source microscopy, synthetic aperture radar.**

I. Introduction

Near-field electromagnetic scanning often is used for root cause diagnosis by determining the field distribution close to the PCB [1]-[3]. The near-field measurement contains both evanescent and radiating fields. In the close vicinity of the device under test (DUT) the evanescent waves are often dominant, which may cause them to be misinterpreted as the dominant contributors to the far-field. Often, engineers focus primarily on the radiating sources of electromagnetic interference (EMI) contributing to far-field radiation. To identify these sources, engineers must depend upon their experience or trial and error approach. Another limitation of near-field scanning is that the probe may not be able to access all locations near the PCB due to the complex geometry and high component density. The measurement of fields at different heights further complicates the interpretation.

To overcome the limitations of near-field scanning in locating EMI radiation sources, the emission source microscopy (ESM) presented in this paper can be used to directly identify the sources of far-field radiation.

Manuscipt received June 10, 2014; revised October 17, 2015; accepted December 19, 2015.

P. Maheshwari was with the EMC Lab, Missouri University of Science and Technology, Rolla, MO 65401 USA. (email: prm8c7@mst.edu).

H. Kajbaf is with the Amber Precision Instruments, San Jose, CA 95124 USA. (email: hamed@amberpi.com)

V. Khilkevich and D. J. Pommerenke are with the EMC Lab, Missouri University of Science and Technology, Rolla, MO 65401 USA (email: khilkevichv@mst.edu; davidjp@mst.edu)

Similar ideas [4]-[5] have been used in the detection of faulty antennas in antenna arrays. The investigators performed two phase-synchronized near-field measurements before applying the synthetic aperture radar (SAR) algorithm to detect faulty antennas. SAR techniques are used mainly for antenna diagnostics and antenna pattern measurements [6]. Another application is the reconstruction of surface currents by scanning very close to the PCB [7]. The method emphasizes capturing the maximum evanescent spectrum to reconstruct the fine details of the surface current distribution. The investigators in [8] demonstrated a method similar to the one presented in this paper for detecting radiating sources, but the paper does not discuss the spectral filtering and spatial sampling requirements. Related techniques also have been used for microwave imaging to detect concealed objects, structural defects, radar and aerial imaging [9]-[11].

The emission source microscopy method presented in this paper derives from the methods employed in [4]-[11]. It is used mainly for localizing radiating EMI sources on complex PCBs or enclosures. The phase and magnitude of the fields are measured on a planar surface a few wavelengths away from the DUT in order to remain outside its reactive near-field region. The scanned fields are back-propagated to the source plane after spectral filtering to identify the radiation sources. Section II presents the analytical formulation of the ESM methodology and then an explanation of how the individual sources can be distinguished. In addition, the total radiated power can be calculated for individual sources to determine the source contributing the most radiation.

Section III explains the phase measurement methodology and discusses how to overcome challenges faced during product scanning. After showing the results of scanning a SI test board, limitations of the method and the parameters that may affect the accuracy of the ESM methodology are discussed.

II. Emission Source Microscopy Algorithm

A. Analytical Formulation of 2D ESM Algorithm

The scanned fields on the observation plane can be expanded using the plane-wave spectrum theory, which states that any monochromatic but otherwise arbitrary field distribution can be represented as a superposition of plane waves travelling in different directions with different amplitudes. According to [12], the electric field intensity in a

source-free region on a plane $(x, y, 0)$ can be represented as a superposition of plane waves in the form of Fourier transform,

$$E(x,y,0) = \frac{1}{4\pi^2}\int_{-\infty}^{\infty}\int_{-\infty}^{\infty} f(k_x,k_y)e^{-j(k_x x+k_y y)}dk_x dk_y \quad (1)$$

where $f(k_x, k_y)$ is the 2-dimensional Fourier transform of $E(x, y, 0)$, as given by,

$$f(k_x,k_y) = \int_{-\infty}^{\infty}\int_{-\infty}^{\infty} E(x,y,0)\, e^{j(k_x x+k_y y)}dxdy \quad (2)$$

Here, k_x and k_y are the spectrum wavenumbers in the x and y directions, respectively. It has been shown [13] that the spectrum of the field on any plane (x, y, z_0) parallel to $(x, y, 0)$ can be found using,

$$f(k_x,k_y,z_0) = f\,(k_x,k_y) * e^{-jk_z z_0} \quad (3)$$

where $k = 2\pi/\lambda$ is the free-space wavenumber, and λ is the wavelength of the active source of radiation. k_z is the z component of the propagation vector given as,

$$k_z = \sqrt{k^2 - k_x^2 - k_y^2}, \quad \text{if } k_x^2 + k_y^2 \le k^2 \quad (4a)$$

$$k_z = -j\sqrt{k_x^2 + k_y^2 - k^2}, \quad \text{otherwise} \quad (4b)$$

Equation (4a) corresponds to the propagating waves whereas equation (4b) corresponds to the evanescent waves.

Therefore, if the field on the scanning plane (x, y, z_0) is known, the field on the source plane $(x, y, 0)$ can be found using,

$$E(x,y,0) = \mathcal{F}^{-1}[\mathcal{F}\{E(x,y,z_0)\} * e^{jk_z z_0}] \quad (5)$$

where 'z_0' is the vertical distance between the planes, and $\mathcal{F}$ and $\mathcal{F}^{-1}$ are the forward and inverse Fourier transform operators, respectively.

Equation (5) allows back-propagation of the field from one plane to another. The fields are usually not available in the form of continuous functions, as in (1) and (2), but instead are sampled at discrete locations. In the case of uniform sampling, (5) would result in discrete rather than continuous Fourier transforms. Equation (5) serves as the basis of the 2-D ESM algorithm. During the transformation (5) the contribution of the evanescent waves can be easily nullified by replacing the exponential factor by 0 when the condition in (4b) is satisfied. This allows to retain information about the radiation component only and eventually obtain the radiation map on the source plane $(x, y, 0)$.

In principle, one can obtain all samples of the field distribution $E(x, y, z_0)$ simultaneously using antenna or probe arrays [14]; however, this is difficult to implement. The potential advantage of using probe arrays is the ability to locate time-varying sources, however on practice the acquisition time of antenna arrays is in the range of milliseconds at best [15], which allows to work with relatively slowly changing fields only.

A more practical approach is to use a moving probe or antenna and sample the field sequentially from point to point. In this case, the scanning plane can be thought of as a synthetic aperture of a large antenna. The disadvantage of this sampling method is that it is limited to non-varying or at least stationary sources, which however represent a very important practical case.

For scanning, the scan plane is divided into a discrete grid of $N \times M$ points. At each point, the tangential electric field components E_x and E_y (or H_x, H_y) are measured. The spatial resolution, Δx and Δy, and the spectral resolution, Δk_x and Δk_y, are related by the following equations,

$$\Delta k_x = \frac{2\pi}{N\Delta x}$$

$$\Delta k_y = \frac{2\pi}{M\Delta x}$$

The distance between the points on the scanning grid should be chosen to be less than $\lambda/2$ in order to satisfy the Nyquist spatial sampling criterion [16]. There are methods allowing to perform the transformation for fields sampled above the Nyquist criterion [17]-[18], however they increase the complexity of the transformation procedure and are not used in this paper.

The resolution of scanning, height of the scanning plane, and frequency of operation affect the final resolution of the back-propagated image. The ESM method (Equation 5) is equivalent to focusing by a lens [32]. The numerical aperture of the lens is given as [19],

$$N.A. = n * \sin\theta \quad (6)$$

where 'n' is the refractive index of the medium, and θ is one-half of the aperture angle in radians, as shown in Fig. 1. Here, 'd' represents the length of the smallest dimension of the physical aperture, and 'h' is the height of the scanning plane above the DUT. Based on the numerical aperture in (6), the resolution of the back-propagated image can be given as,

$$R = \lambda/(2 * N.A.) \quad (7)$$

Equation (7) sets the limit for the resolution that can be achieved in the back-propagated image. For an infinitely wide scanning aperture, the aperture angle would be 90 degrees, and with air as the medium, the maximum N.A. would be 1. This limits the theoretical maximum resolution to $\lambda/2$, which is also the diffraction limit of optical (and microwave) microscopy.

B. Method validation on a custom PCB

To test the usefulness of the ESM method for EMC applications, a custom PCB with several patches and traces

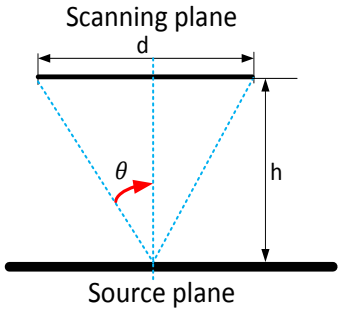

Fig. 1. Aperture angle given by the span of the scan plane.

was built. Fig. 2 shows the full-wave model of the PCB built in the CST microwave studio [21]. The model was used to compare the experimental and simulation results

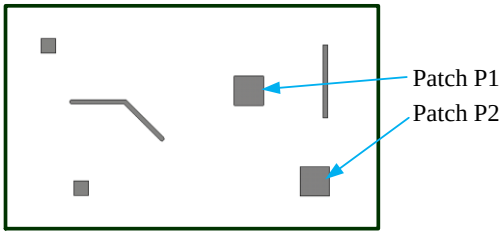

Fig. 2. Model of the custom PCB.

The PCB was 254 mm x 152 mm in size and had two 20 x 20 mm center-fed patches. The simulation assumed a perfect electric conductor (PEC) for metal layers and FR-4 (ε_r = 4.3) for dielectric material. During the simulation, patches P1 and P2 were excited simultaneously at 8.2 GHz. Using the time-domain solver in CST, the complex tangential electric fields E_x and E_y were simulated at a height of 2λ (73.2 mm) above the DUT plane, as shown in Figs. 3 and 4. To compare these simulated results to the measurement results, the field magnitudes were normalized to a 1 V input excitation.

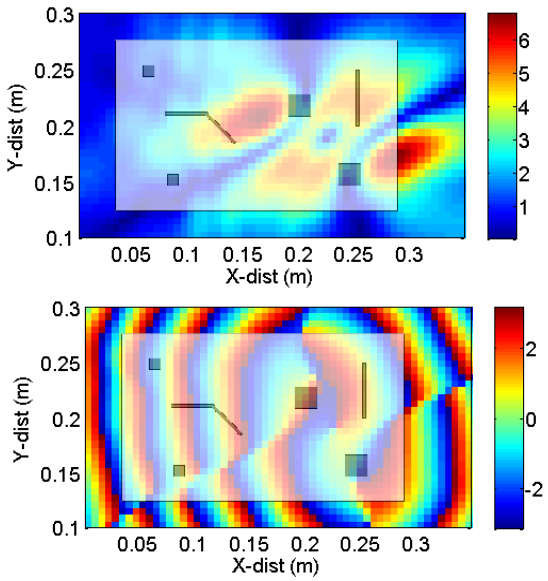

Fig. 3. Simulated $\boldsymbol{E_x}$ field magnitude (V/m) (top) and phase (rad) (bottom) on the scanning plane at 73.2 mm above the DUT using full-wave simulation.

The image of the DUT was overlapped and aligned with the image of the scanned fields to allow an observation of the underlying physical sources of radiation. As Figs. 3 and 4 indicate, observing the fields simulated at 2λ yielded no particularly useful information about the source of radiation. However, when the ESM algorithm given in (5) was applied to the simulated fields (with evanescent wave suppression), and the back-propagated field on the PCB plane was obtained, the sources were localized easily. The back-propagated field on the source plane for both orientations appears in Figs. 5 and 6.

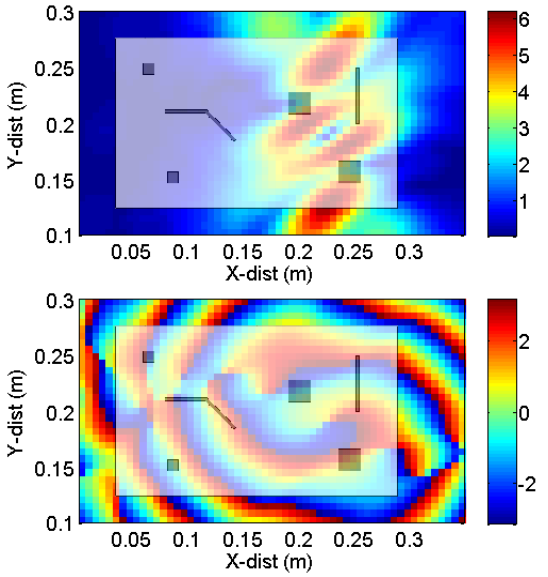

Fig. 4. Simulated $\boldsymbol{E_y}$ field magnitude (V/m) (top) and phase (rad) (bottom) on the scanning plane at 73.2 mm above the DUT using full-wave simulation.

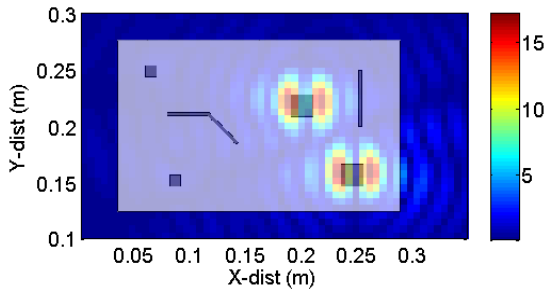

Fig. 5. Back-propagated $\boldsymbol{E_x}$ field magnitude (V/m) on the source plane.

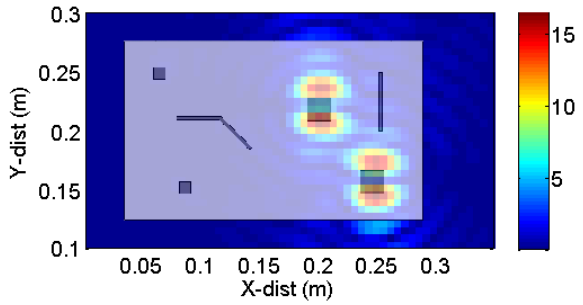

Fig. 6. Back-propagated $\boldsymbol{E_y}$ field magnitude (V/m) on the source plane.

The resolution of the back-propagated image, as calculated using (7), is approximately 1.9 cm. The edge-to-edge separation between the patches is 4.8 cm, i.e. above the theoretical resolution limit, which agrees with the obtained image maps. The ripples in the back-propagated images around the sources are diffraction rings, which are common in optical microscopy.

C. Measurement Results for Custom PCB

For measurement, an X-band open-ended waveguide with a usable frequency range of 8.2-12.4 GHz was used as a scanning antenna. It was moved in a uniform rectangular grid over the custom PCB using an API 3-axis EMI scanning system [22]. The patches were excited simultaneously at 8.2 GHz. A vector network analyzer (VNA) was used to measure the amplitude and phase of the scanned fields. Port 1 of the VNA fed a resistive splitter to excite patches P1 and P2, while Port 2 of the VNA was connected to the scanning antenna to receive the radiated signal. The calibration of the VNA was performed up to the input of the patches in order to compensate for the loss of the splitter. The S_{21} obtained using the VNA provided the amplitude and phase of the fields over the scanning plane.

The output of the scanning antenna is a convolution of the fields received at the aperture and the probe response [30]. To obtain the actual fields existing at the probe locations, the probe response must be removed using a procedure called probe correction. This can be accomplished in the spectrum domain by dividing the spectrum of the received probe output by the spectrum of the probe response. In the case of an open-ended waveguide, the beam width is relatively large, so the far-field antenna factor of the open-ended waveguide was used as a first-order approximation for the probe response. The antenna factor was calculated analytically. After applying the antenna factor, the measured S_{21} values can be considered as the fields from the patches in response to a 1 V input excitation. This allows the measurement fields to be compared to the simulated results.

To apply the ESM algorithm, the fields emitted by the sources are measured on a planar surface at a certain distance above the DUT. Here, the distance was kept at 2λ (73.2 mm) so that the results could be compared with those from the full-wave simulation. The spatial scanning resolution was kept at $\lambda/6$, which resulted in 1800 sampling points. Figs. 7 and 8 depict the measured fields for both polarizations after applying the probe correction. After applying the ESM algorithm to the measured data and reconstructing the image from the source plane, the sources were identified in both orientations, as shown in Figs. 9 and 10. As can be seen, the obtained images are very close to those obtained in simulation (Fig 5 and 6) in both pattern and magnitude.

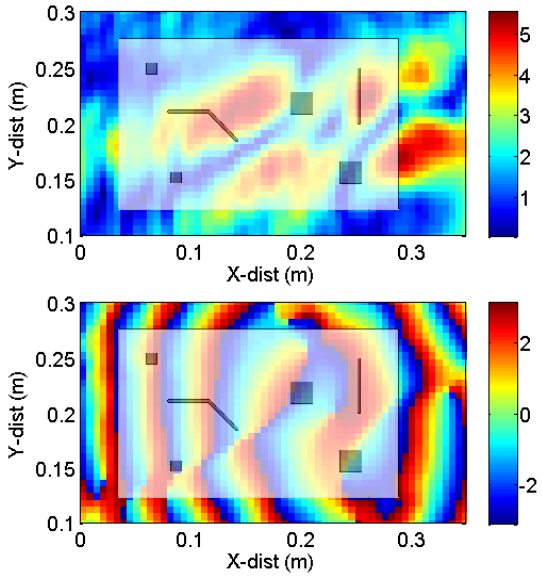

Fig. 7. Measured $\boldsymbol{E_x}$ field magnitude (V/m) (top) and phase (rad) (bottom) on the scanning plane at 73.2 mm above the DUT.

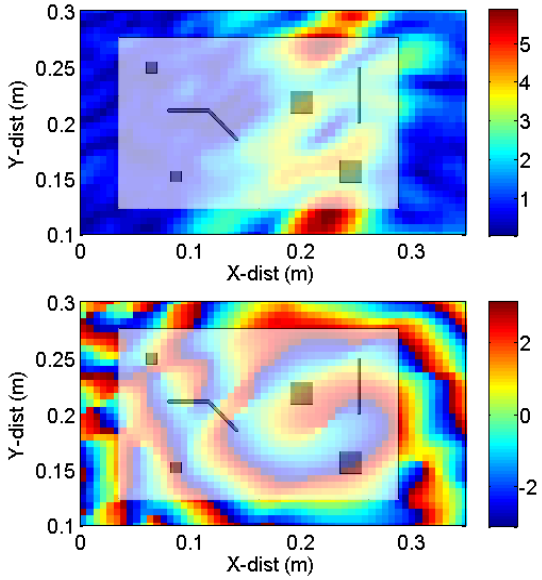

Fig. 8. Measured $\boldsymbol{E_y}$ field magnitude (V/m) (top) and phase (rad) (bottom) on the scanning plane at 73.2 mm above the DUT.

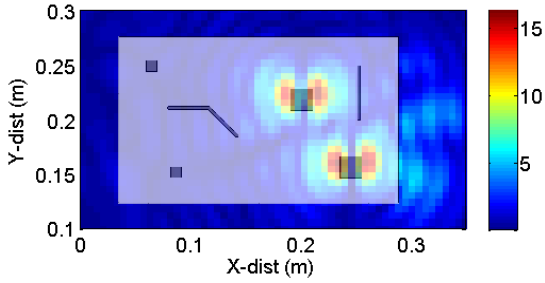

Fig. 9. Back-propagated $\boldsymbol{E_x}$ field magnitude (V/m) on the source plane.

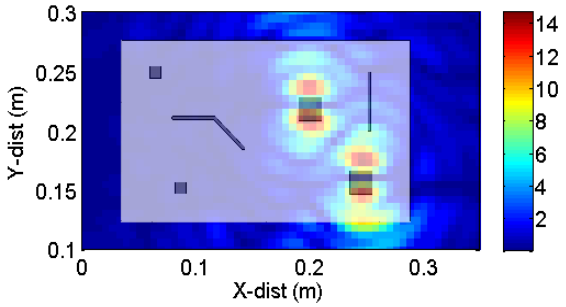

Fig. 10. Back-propagated $\boldsymbol{E_y}$ field magnitude (V/m) on the source plane.

D. Near-field to far-field transformation calculation

The next step is to calculate the far-field pattern of the sources identified on the source plane. This provides information such as the maximum radiated emission and the total radiated power from the DUT, eliminating the need to perform complicated measurements in the anechoic chamber. On the other hand neglecting the field outside the rectangular scanning region (which is inevitable) affects the accuracy of the computed far-field [27], which makes it essential to define the scanning region sufficiently large to capture as much information about the EMI sources and possible.

To interpolate in the frequency domain, the field data in the spatial domain are zero-padded before conversion to the spatial spectrum domain. The plane wave spectra $f_x(k_x, k_y)$ and $f_y(k_x, k_y)$ can be used to calculate the far-field using the stationary phase method [12],

$$E_\theta(r,\theta,\phi) \approx j\frac{ke^{-jkr}}{2\pi r}(f_x cos\phi + f_y sin\phi) \tag{8}$$

$$E_\phi(r,\theta,\phi) \approx j\frac{ke^{-jkr}}{2\pi r}cos\theta\,(-f_x sin\phi + f_y cos\phi) \tag{9}$$

Angles θ and ϕ in Equations (8) and (9) can be obtained from k_x and k_y by solving the system of equations

$$k_x = ksin\theta cos\phi$$
$$k_y = ksin\theta sin\phi.$$

Firstly, the far-field was computed from the data obtained in simulation, as shown in Fig. 11. The far-field pattern was determined in a similar manner from the scanned data obtained via measurement, as shown in Fig. 12. The 3D field patterns from the measured data and from the simulation results appear to agree reasonably well. The maximum value of component E_θ obtained from the simulation was 1.7 dBV/m, as compared to 2.7 dBV/m from the measurement data. This is the maximum peak value of the far-field in the entire sphere, so the angle is not specified.

The total radiated power can be computed from the radiation intensity, which can be given as,

$$U(\theta,\phi) = \frac{r^2}{2\eta}\left[|E_\theta(r,\theta,\phi)|^2 + \left|E_\phi(r,\theta,\phi)\right|^2\right]. \tag{10}$$

The total radiated power can be obtained by integrating the radiation intensity over the hemisphere,

$$P_{rad} = \oiint_{\Omega} U \, d\Omega = \int_0^{2\pi} \int_0^{\pi} U \, sin\theta \, d\theta \, d\phi \quad (11)$$

where dΩ is an element of the solid angle that equals sinθ dθ dϕ.

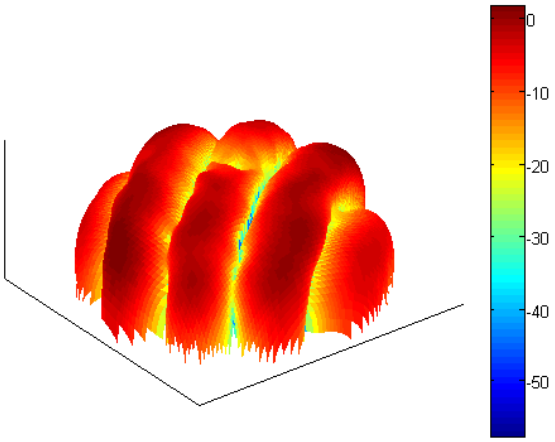

Fig. 11. Far-field pattern for component $\boldsymbol{E_\theta}$ in dBV/m from simulation.

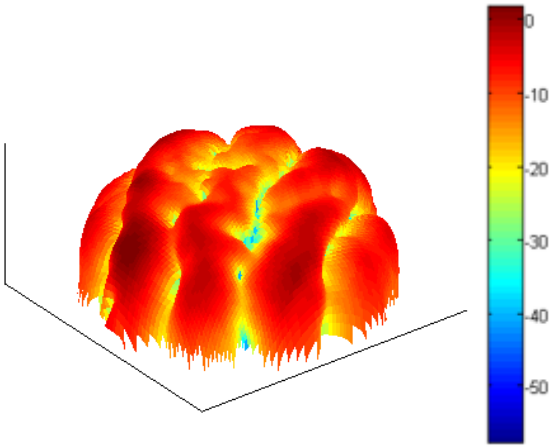

Fig. 12. Far-field pattern for component $\boldsymbol{E_\theta}$ in dBV/m from measurement.

The numerical integration over the 2D surface can be evaluated using Simpson's rule [25]. The total radiated power calculated was 6.3 dBm using the measurement data. The total radiated power obtained from full-wave simulation for the two patches was 7.04 dBm. This shows that the back-propagated fields on the source plane can be used to predict the total radiated power of the DUT with accuracy sufficient for most EMC applications. Of course, the transformation to the far-field can be performed directly from the scanned data without the intermediate back-propagation step. The back-propagation however allows to calculate the contributions of individual sources, which is discussed in the next section.

E. Determining Contributions from Individual Sources

As seen in Fig. 6, the two sources were identified on the source plane using the ESM method. Often it is interesting to estimate the far-field contribution of each individual EMI source. This can be achieved by masking the ESM image (i.e. nullifying the field outside a certain region associated with the source) to remove contributions of other unwanted sources and then performing the near-field to far-field transformation as described above. An example of masking the ESM image on fig. 9 and 10 to estimate the contribution of the patch P1 is shown in Fig. 13.

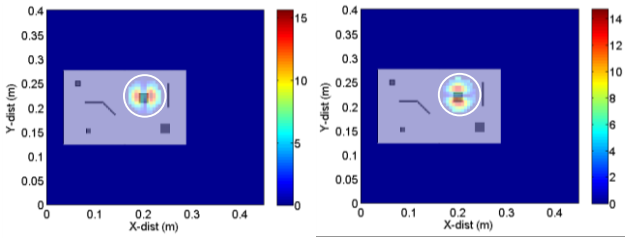

Fig. 13. Back-propagated $\boldsymbol{E_x}$ (left) and $\boldsymbol{E_y}$ (right) field magnitudes (V/m) on the source plane from scanned data with sources masked. The masks are showed as white circles.

The maximum value of component E_θ obtained from the simulated fields was -6.0 dBV/m, whereas the scanned fields yielded a maximum value of -5.2 dBV/m. Also, the total radiated power from the simulated fields for the source corresponding to patch P1 was 1.96 dBm, whereas the measurement yielded a value of 1.19 dBm. This result indicates that after the sources are localized on the source plane using the ESM methodology, contributions from individual sources can also be calculated with sufficient accuracy for most EMC applications.

III. Application of ESM Methodology on an Active DUT

The application of the ESM methodology on an active DUT is presented in this section. For this method to work, the amplitude and phase of the electromagnetic field must be measured. The literature describes different phase measurement methods, including a time-domain method [23] and a spectrum analyzer based method [24]. The drawback of the latter method is that it requires three scans to retrieve the phase information. On the other hand in the time domain, the sample frequency must be relatively high. For example if no down-mixing is used, a 20 GS/sec sampling rate will be required at 8.2 GHz.

A further complication of the time domain method results from the relationship between the recorded length and the spectral resolution. If the sources have multiple frequency components, the method must distinguish between them. This could result in the need for a very long time record. To overcome the drawbacks of the above two methods, the phase and magnitude were measured using a vector network analyzer (VNA) in tuned receiver mode.

In tuned receiver mode, the internal RF source is turned off and the VNA measures the amplitudes of each receiving channel signals at the set frequency and the phase difference between them. A phase reference signal is needed, which can be obtained either by using a stationary antenna pointed on the DUT or by tapping into the DUT being measured. The other port of the VNA is connected to the scanning antenna. The phase difference between the reference and the measurement channels provides the phase value for the scanned fields. The amplitude from the scanning antenna is measured directly.

A. Phase measurement setup and algorithm

An off-the-shelf FPGA transceiver board [31] operating at the clock frequency of 3.125 GHz was used as a DUT. The FPGA was programmed to output a differential clock signal on one of the differential channels. At the clock frequency, the achievable spatial resolution was 5 cm (calculated using (7)). At the third harmonic, 9.375 GHz, the resolution improved, reaching 1.56 cm. This resolution limit is less than the distance between the adjacent SMA connectors on the board and thus allows for radiating structure to be identified in this example. So, this value was selected as the test frequency. The clock signal was outputted at two SMA connectors, as shown in Fig. 16.

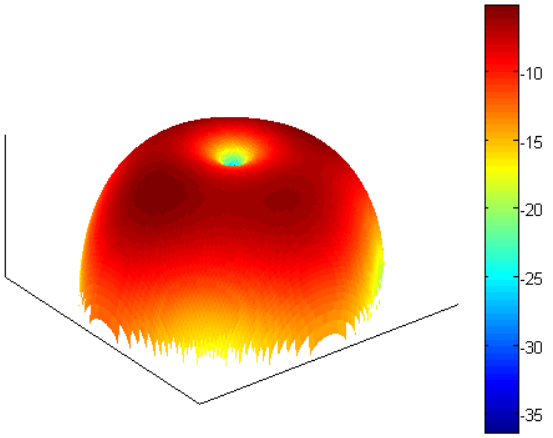

Fig. 14. Far-field pattern for $\boldsymbol{E_\theta}$ component in dBV/m from back-propagated masked fields using simulated data.

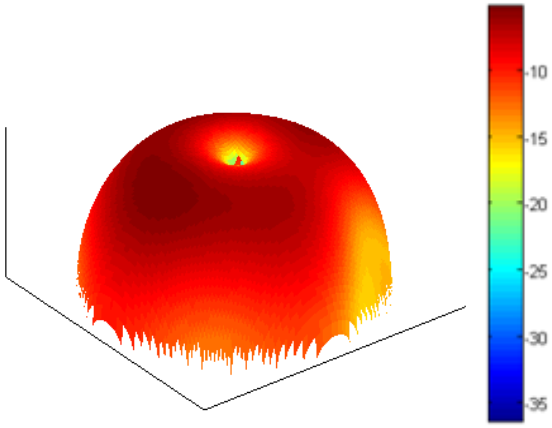

Fig. 15. Far-field pattern for $\mathbf{E_\theta}$ component in dBV/m from back-propagated masked fields using scanned data.

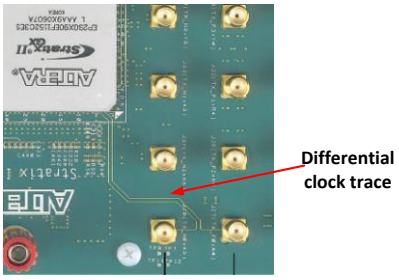

Fig. 16. Differential clock trace feeding into open SMA connectors on the FPGA transceiver board.

Fig. 17 illustrates the measurement setup. An open-ended X-band waveguide served as the scanning antenna. It is moved by an API 3-axis EMI scanning system [22]. The reference signal required for phase measurement was obtained by tapping the right SMA connectors of the differential clock line. The left SMA connector was not terminated. The scanning step was kept at 7 mm in both the x and y directions.

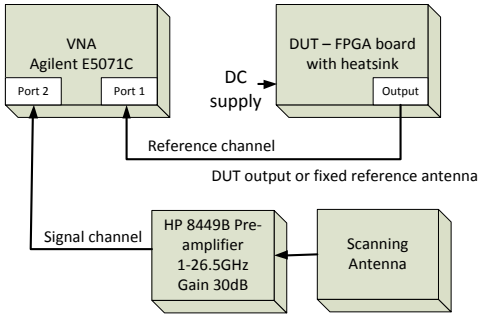

Fig. 17. Measurement setup for tuned receiver mode.

The VNA was centered on the desired frequency and operated in zero span mode. The number of sweep points was set to 100 to obtain an average of the measured signal, which improves the signal-to-noise ratio. The IF bandwidth was kept at 300 Hz. The settings were determined as a trade-off between the sweep time, the signal-to-noise ratio, and the need to accommodate the frequency drift of the signal emitted by the DUT. A larger IF bandwidth would have allowed to capture the signal without having to track the thermally drifting frequencies of the DUT, however, the signal to noise ratio would have not been sufficient.

Every 100 spatial scan points, the drift compensation routine changed the VNA span from 0 Hz to 500 kHz and searched for the exact peak corresponding to the desired frequency. It then designated it again as the center frequency and continued the measurement.

Fig. 18 shows the magnitude of the total tangential electric field $E_t = \sqrt{\left(E_x^2 + E_y^2\right)}$, and Fig. 19 shows the phase of the E_x component. The data indicate that limited information about the sources of radiation can be obtained from the scanned fields.

To demonstrate the advantages of the ESM technique over a conventional near-field scan, the near-field was measured using a 2 mm loop probe at a height of 0.5 mm above the PCB surface with the step of 3 mm. Only the field magnitude was measured. The result of the near-field scanning appears in Fig. 20, where the active differential trace is clearly visible, however no radiation form the heat sink and open SMA connector can be seen.

Using the fields measured at a distance of 5 cm, the ESM technique was applied, and the fields were back-propagated to the source plane. The back-propagated fields on the source plane appear in Fig. 21, which indicates two sources of radiation – one related to the FPGA heat sink and the other related to the open SMA connector. The evanescent field components associated with the microstrip transmission line are completely suppressed (compare fig. 21 to fig. 20). The possible reason for the relatively strong radiation from the heat sink is the asymmetric termination of the differential transmission line, creating strong common mode exciting the heat sink. In order to verify this hypothesis, the open SMA connector was terminated using a 50 ohm termination, which drastically reduced the common mode current on the

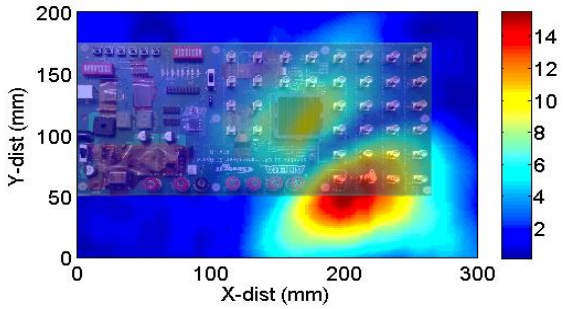

Fig. 18. Measured field magnitude (V/m) on the scanning plane at 5 cm above the DUT.

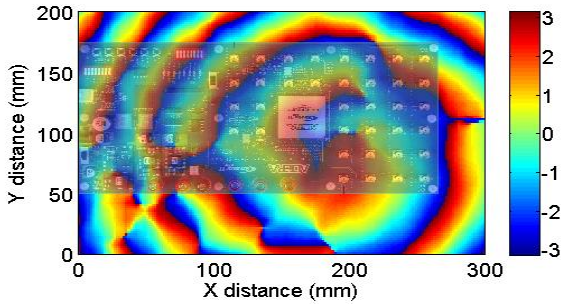

Fig. 19. Measured field phase (rad) on the scanning plane at 5 cm above the DUT.

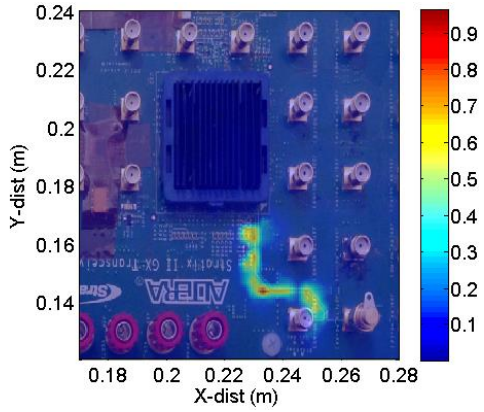

Fig. 20. Measured tangential fields (magnitude) for the FPGA board using near-field scanning.

differential clock trace and thus the resulting radiation. The back-propagated field on the source plane with symmetrical termination of the differential clock line appears in Fig. 22. The same scale in fig. 21 and 22 allows to visually compare the radiation intensity observed with asymmetrical and symmetrical termination of the differential line.

For the case with the matched load, the total radiated power decreased by 7.36 dB relative to the case with asymmetrical termination as predicted by the ESM scans. To validate the reduction in the total radiated power, measurements according to [26] were performed in a reverberation chamber with and without the matched load. The measurement showed a reduction of 6-7 dB which agrees well with the ESM prediction.

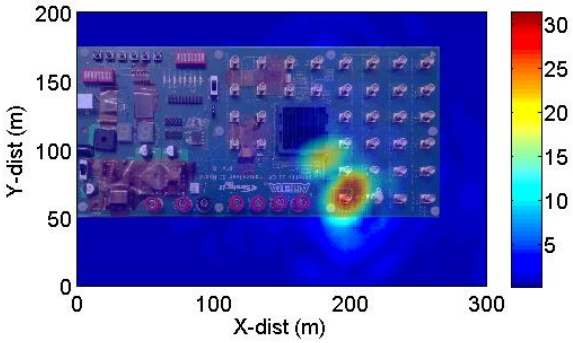

Fig. 21. Back-propagated field magnitude (V/m) on the source plane with left SMA connector kept open and the right one loaded by a matched load (VNA port).

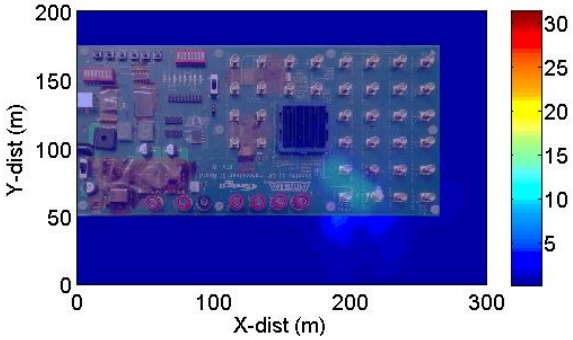

Fig. 22. Back-propagated field magnitude (V/m) on the source plane with both connectors loaded by matched terminations.

B. Discussions and challenges

The ESM method shows the field distribution of the active sources on the source plane corresponding to the propagating waves only. Its main limitation is the resolution of the back-propagated image on the source plane, as given by Equation (7). This limits the usage of the method at lower frequencies where wavelength might become comparable to the size of the DUT. Another limitation of the method is that it requires phase measurement. Table 1 compares near-field scanning and the proposed ESM method.

Parameters	**ESM scanning**	**Near-field scanning**
Image resolution	Limited by wavelength and aperture	Limited by the probe size, probe to source distance and scanning spatial step
Phase measurement	Required	Magnitude information usually sufficient
Scanning distance	Possible to scan a few wavelengths away	As close as possible to DUT
Data	Information about radiating sources only	Both evanescent and propagating fields are obtained

Table 1 Comparison of scanning methods

The accuracy of the ESM method is limited in several ways. The limited range of the scanning hardware causes the measurement plane to be truncated. The aperture diffraction rings and the effect of truncation can be minimized by windowing techniques [17], [28] and [29], but cannot be eliminated completely. Uncorrelated amplitude and phase noise received by the scanning antenna might affect the accuracy of the overall measurement. Other factors, such as the cable transmission coefficient variation, back scattering from the antenna, limited dynamic range of the receiver, and insufficient image channel rejection of the super heterodyne receiver, also affect the accuracy of the measurement.

IV. CONCLUSION

An important step in mitigating EMI involves identifying the sources of radiation on the DUT. The ESM methodology presented in this paper can help to localize the sources of radiation on the PCB. After the radiating sources are located, individual sources can be distinguished and identified. Using masking algorithms, far-field contributions from individual sources can be calculated. It was shown that the total radiated power and maximum field from each source can be estimated with good accuracy (approximately 1 dB). Once the dominant source of EMI is identified, an appropriate EMI mitigation method can be applied to reduce the radiated emissions with immediate control of the achieved EMI reduction.

REFERENCES

[1] X. Dong, S. Deng, T. Hubing, D. Beetner, "Analysis of chip-level EMI using near-field magnetic scanning," *International Symposium on Electromagnetic Compatibility*, vol. 1, pp. 174-177, 9-13 Aug. 2004.

[2] J. Shi, M.A. Cracraft, J. Zhang, R.E. DuBroff, K. Slattery, "Using near-field scanning to predict radiated fields," *International Symposium on Electromagnetic Compatibility*, vol. 1, pp.14-18, 9-13 Aug. 2004.

[3] J.J.H. Wang, "An examination of the theory and practices of planar near-field measurement," *IEEE Transactions on Antennas and Propagation*, vol. 36, no. 6, pp. 746-753, Jun. 1988.

[4] P.L. Ransom, R. Mitra, "A method of locating defective elements in large phased arrays," *Proc. of the IEEE*, vol. 59, no. 6, pp. 1029-1030, Jun. 1971.

[5] J.J. Lee, E.M. Ferren, D.P. Woollen, K.M. Lee, "Near-field probe used as a diagnostic tool to locate defective elements in an array antenna," *IEEE Transactions on Antennas and Propagation*, vol. 36, no. 6, pp. 884-889, Jun. 1988.

[6] K.S. Farhat, N. William, "Microwave holography applications in antenna development," *IEE Colloquium on Novel Antenna Measurement Techniques*, pp. 3/1, 3/4, 26 Jan. 1994.

[7] P.H. Harms, J.G. Maloney, M.P. Kesler, E.J. Kuster, G.S. Smith, "A system for unobtrusive measurement of surface currents," *IEEE Antennas and Propagation Society International Symposium*, vol. 3, pp. 1646-1649, 21-26 Jun. 1998.

[8] H. Hirayama, T. Yakabe, Y. Kami, "An imaging system for EM emitting sources using a 6-port correlator," *IEEE International Symposium on Electromagnetic Compatibility*, vol. 1, pp. 374-37, 2001.

[9] D. Sheen, D. McMakin, T. Hall, "Three-dimensional millimeter-wave imaging for concealed weapon detection," in *IEEE Transactions on Microwave Theory and Techniques*, vol. 49, no. 9, Sep. 2001.

[10] M. Fallahpour, J.T. Case, M. Ghasr, R. Zoughi, "Piecewise and Wiener filter-based SAR techniques for monostatic microwave imaging of layered structures," in *IEEE Transactions on Antennas and Propagation*, vol. 62, no. 1, pp. 1-13, Jan. 2014.

[11] M. Fallahpour, M. Ghasr, J.T. Case, R. Zoughi, "A Wiener filter-based synthetic aperture radar (SAR) algorithm for microwave imaging of targets in layered media," in *Materials Evaluation*, vol. 69, no. 10, pp. 1227-1237, Oct. 2011.

[12] C.A. Balanis, "Antenna theory: Analysis and design," 3rd Edition, Apr. 2005.

[13] A.D. Yaghjian, "An overview of near-field antenna measurements," *IEEE Transactions on Antennas and Propagation*, vol. ap-34, no. 1, Jan. 1986.

[14] W.M. Brown, "Synthetic aperture radar," *IEEE Transactions on Aerospace and Electronic Systems*, vol. AES-3, no. 2, pp. 217-229, Mar. 1967.

[15] M.T. Ghasr, M.A. Abou-Khousa, S. Kharkovsky, R. Zoughi, D. Pommerenke, "Portable real-time microwave camera at 24 GHz," *IEEE Transactions on Antennas and Propagation*, vol. 60, no. 2, pp. 1114-1125, Feb. 2012.

[16] J.T. Case, M.T. Ghasr, R. Zoughi, "Optimum two-dimensional uniform spatial sampling for microwave SAR-based NDE imaging," *IEEE Transactions on Instrumentation and Measurement*, vol. 60, no. 12, pp. 3806-3815, Dec. 2011.

[17] H. Kajbaf, J.T. Case, Z. Yang, Y.R. Zheng, "Compressed sensing for SAR-based wideband three-dimensional microwave imaging system using non-uniform fast Fourier transform," *Radar, Sonar & Navigation*, IET, vol. 7, no. 6, pp. 658-670, Jul. 2013.

[18] H. Kajbaf, J.T. Case, Y.R., Zheng, S. Kharkovsky, R. Zoughi, "Quantitative and qualitative comparison of SAR images from incomplete measurements using compressed sensing and nonuniform FFT," *IEEE Radar Conference (RADAR)*, pp. 592-596, May 2011.

[19] M. Abramowitz, M.W. Davidson, "Microscope objectives: Numerical aperture and resolution," *Molecular Expressions: Optical Microscopy Primer* (website), Florida State University, Apr. 2004.

[20] J.D. Hanfling, G. Borgiotti, L. Kaplan, "The backward transform of the near field for reconstruction of aperture fields," *Antennas and Propagation Society International Symposium*, vol. 17, pp. 764-767, Jun. 1979.

[21] CST Microwave studio. [Online]. Available: http://www.cst.com

[22] G. Muchaidze, J. Koo, Q. Cai, T. Li, L. Han, A. Martwick, K. Wang, J. Min, J.L. Drewniak, D. Pommerenke, "Susceptibility scanning as a failure analysis tool for system-level electrostatic discharge (ESD) problems," *IEEE Transactions on Electromagnetic Compatibility*, vol. 50, no. 2, pp. 268-276, May 2008.

[23] Y. Vives-Gilabert, C. Arcambal, A. Louis, D.F. Daran, P. Eudeline, B. Mazari, "Modeling magnetic radiations of electronic circuits using near-field scanning method," *IEEE Transcations on Electromagnetic Compatibility*, vol. 49, no. 2, pp. 391-400, May 2007.

[24] J. Zhang, K.W. Kam, J. Min, V.V. Khilkevich, D. Pommerenke, J. Fan, "An effective method of probe calibration in phase-resolved near-field scanning for EMI application," *IEEE Transactions on Instrumentation and Measurement*, vol. 62, no. 3, pp. 648-658, Mar. 2013.

[25] J.L. Volakis, D.B. Davidson, "Calculating directivities with the two-dimensional Simpson's rule," *IEEE Antennas and Propagation Magazine*, vol. 46, no. 4, pp. 106-112, Aug. 2004.

[26] G. Koepke, J. Ladbury, "Radiated power measurements in reverberation chambers," *56th ARFTG Conference Digest-Fall*, vol. 38, pp. 1-7, Nov. 2000.

[27] X. Ren, P. Maheshwari, et al. "The impact of near-field scanning size on the accuracy of far-field estimation," in *IEEE Symposium on Electromagnetic Compatiblity*, 2014.

[28] I.G. Cumming, F.H. Wong, "Digital processing of synthetic aperture radar data: algorithms and implementation," published by Artech House, 2005.

[29] A.V.Oppenheim, R.W. Schafer, "Discrete-time signal processing," published by Prentice-Hall, New Jersey, USA, 2010.

[30] H. Wang, D.G. Beetner, R.E. Dubroff, "Frequency-domain probe characerterization and compensation using reciprocity," in *IEEE Transactions on Electromagnetic Compatiblity*, vol. 53, pp. 2-10, 2010.

[31] Website: www.altera.com, "Startix II GX EP2SGX90 Transreceiver SI development board," ver 1.0.0, May 2006.

[32] Introduction to Fourier Optics. JOSEPH W. GOODMAN. McGraw-Hill, New York, 1968.

Pratik Maheshwari received the B.E. degree in electronics engineering in 2008 from the University of Mumbai, India. He received his PhD degree in August 2014. His research interests include EMI source localization, electrostatic discharge, and RF system design.

Victor Khilkevich received the PhD degree in electrical engineering from the Moscow Power Engineering Institute, Technical University, Moscow, Russia, in 2001.

He is currently an Assistant Professor at the Missouri University of Science and Technology, Rolla MO USA. His primary research interests include microwave imaging, automotive electromagnetic compatibility modeling, and high-frequency measurement techniques.

Hamed Kajbaf received the BS degree in electrical engineering from Shiraz University, Shiraz, Iran, in 2006, the MS degree in biomedical engineering-bioelectric from Tarbiat Modares University, Tehran, Iran, in 2009. He received his PhD degree in electrical engineering from Missouri University of Science and Technology, Rolla, MO, USA, in 2012.

He is currently an EMC engineer at Amber Precision Instruments Inc. (API), San Jose, CA. His research interests include microwave and EMC scanning systems, near-field electromagnetic and acoustic imagining, RF measurements and instrumentation optimization, and array signal processing.

David Pommerenke received a PhD degree from the Technical University Berlin, Berlin, Germany, in 1996. After working at Hewlett Packard for five years, he joined the EMC Laboratory at the University of Missouri-Rolla, Rolla, in 2001, where he is currently a Professor. He has published more than 200 papers and is an inventor on 13 patents. He researches EMC with an emphasis on measurement and instrumentation, electronics, and immunity of electronic circuits, such as electrostatic discharge.